

# Phase transitions between helices, vortices, and hedgehogs driven by spatial anisotropy in chiral magnets

Kotaro Shimizu, Shun Okumura, Yasuyuki Kato, and Yukitoshi Motome  
*Department of Applied Physics, The University of Tokyo, Tokyo 113-8656, Japan*  
(Dated: November 2, 2020)

Superpositions of spin helices can yield topological spin textures, such as two-dimensional vortices and skyrmions, and three-dimensional hedgehogs. Their topological nature and spatial dimensionality depend on the number and relative directions of the constituent helices. This allows mutual transformation between the topological spin textures by controlling the spatial anisotropy. Here we theoretically study the effect of anisotropy in the magnetic interactions for an effective spin model for chiral magnetic metals. By variational calculations for both cases with triple and quadruple superpositions, we find that the hedgehog lattices, which are stable in the isotropic case, are deformed by the anisotropy, and eventually changed into other spin textures with reduced dimension, such as helices and vortices. We also clarify the changes of topological properties by tracing the real-space positions of magnetic monopoles and antimonopoles as well as the emergent magnetic field generated by the noncoplanar spin textures. Our results suggest possible control of the topological spin textures, e.g., by uniaxial pressure and chemical substitution in chiral materials.

## I. INTRODUCTION

Chiral magnets with noncentrosymmetric crystal structures often show interesting spin textures through the spin-orbit coupling. In these systems, the spin-orbit coupling generates an effective antisymmetric exchange interaction, called the Dzyaloshinskii-Moriya (DM) interaction [1, 2], which twists the spin configuration. The simplest example is a helical structure shown in Fig. 1(a) [3–6]. There are, however, a variety of noncollinear and noncoplanar spin textures composed of superpositions of the helices. Several examples are shown in Fig. 1: a vortex crystal (VC) [Fig. 1(b)] [7–9], a skyrmion lattice (SkL) [Fig. 1(c)] [10–12], and hedgehog lattices (HLs) [Figs. 1(d) and 1(e)] [13, 14]. The wave vectors of the constituent helices are shown in each inset. The VC and SkL have two-dimensional swirling spin textures composed of two and three helices, respectively, whose wave vectors are on the same plane, while the two different types of the HLs have three-dimensional textures composed of three and four helices spanning in three dimensions. The SkL has been found in the wide range of materials, such as B20 compounds (MnSi [10, 12], FeGe [15], and  $\text{Fe}_{1-x}\text{Co}_x\text{Si}$  [11, 16]), multiferroic insulator  $\text{Cu}_2\text{OSeO}_3$  [17, 18], and  $\beta$ -Mn type Co-Zn-Mn alloys [19]. The HL composed of three helices, which we call 3Q-HL, was observed in the B20 compound MnGe [20]. The other type of HL composed of four helices called 4Q-HL was also discovered in  $\text{MnSi}_{1-x}\text{Ge}_x$  ( $0.3 \leq x \leq 0.6$ ) [13]. Interestingly, the VC was recently observed in a centrosymmetric magnet  $\text{GdRu}_2\text{Si}_2$  [9], suggesting other stabilization mechanism rather than the DM interaction. We also note that the 4Q-HL was found in the centrosymmetric cubic perovskite  $\text{SrFeO}_3$  [21].

These spin textures affect the electronic state of the system in several ways. One is in the spatial dimensionality inherited from the magnetic textures: The helical structure in Fig. 1(a) has a one-dimensional modulation, the VC in Fig. 1(b) and the SkL in Fig. 1(c) have two-

dimensional ones, and the HLs in Figs. 1(d) and 1(e) have three-dimensional ones. The difference in the dimensionality yields the corresponding anisotropy in the electronic state. Another way is in the quantum phase of the electron wave function, which is called the Berry phase [22]. Itinerant electrons coupled with these noncollinear and noncoplanar spin textures feel an emergent electromagnetic field through the Berry phase, and exhibit unconventional transport and optical responses [23, 24]. In addition, some of the spin textures have topologically nontrivial structures, which are robust against continuous deformation and characterized by topological numbers. For instance, the SkL is characterized by the so-called skyrmion number, and the HLs are by the monopole charges [25–27]. In particular, the HLs are regarded as a periodic array of hedgehog- and antihedgehog-like spin textures that are sources and sinks of the emergent magnetic field (monopoles and antimonopoles), respectively. Such topological nature is also relevant to the electronic properties [26, 28, 29].

The question that we address in this study is how to control the spin textures with different dimensionality and topology. Once one can switch them from one to another, it may be able to manipulate not only the magnetism but also the electronic state, transport, and optical responses. An example of such a control was found in a certain class of chiral magnets, e.g., the B20 compounds, by applying a magnetic field; the one-dimensional helical state at zero field is changed into a two-dimensional SkL in an applied field [10–12], and correspondingly, the system exhibits an unconventional Hall effect, which is called the topological Hall effect, due to the effective magnetic field arising from the topological noncoplanar spin texture in the SkL. Similar switching was achieved by spatial geometry and anisotropy; a conical state in a bulk sample is taken over by the SkL in thin films [12, 15, 30]. In addition, interesting transitions among helical, SkL, and HLs were discovered in  $\text{MnSi}_{1-x}\text{Ge}_x$  by chemical substitution [13]. Such in-

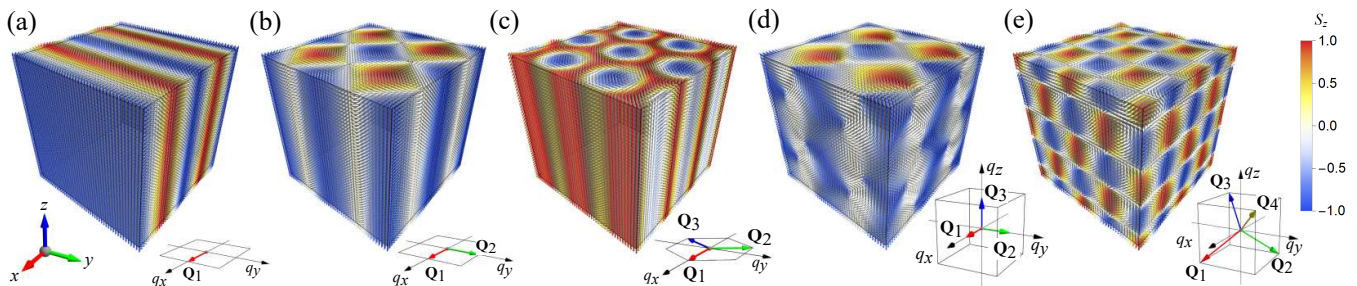


FIG. 1. Real-space spin configurations of (a) a helical state (1Q-H), (b) a vortex crystal composed of two helices (2Q-VC), (c) a skyrmion lattice composed of three (SkL), (d) a hedgehog lattice composed of three (3Q-HL) and (e) another hedgehog lattice composed of four (4Q-HL). The arrows represent the spins and their colors display the  $z$  component. Each inset shows the wave vectors of the constituent helices.

interesting possibilities to control the dimensionality and topology, however, have not been systematically investigated thus far, especially including the three-dimensional HLs.

In this paper, we theoretically study such a control of the spin textures focusing on the effect of spatial anisotropy. For an effective spin model with long-range interactions stemming from itinerant nature of electrons [31], we clarify the ground-state phase diagram by variational calculations while changing the anisotropy in the interactions. We find that the HLs, which are stable in the isotropic case, change their magnetic textures with dimensional reduction by the anisotropy. In the 3Q-HL case, the three-dimensional magnetic texture turns into a two-dimensional VC for the hard-axis anisotropy along the helix direction, while into another type of VC and eventually a one-dimensional helical state for the easy-axis anisotropy. Meanwhile, the 4Q-HL changes into the 3Q-HL and a helical state for the hard- and easy-axis anisotropy, respectively. Tracing the spatial positions of the hedgehogs and antihedgehogs, we find several types of topological transitions with their creation and annihilation while changing the anisotropy. We also clarify how the flow of the emergent magnetic field is modulated through the phase transitions. Our results demonstrate that the spatial anisotropy is useful to control not only the magnetic structures including their dimensionality but also electric, transport, and optical properties arising from the topological nature through the emergent magnetic field.

The rest of the paper is organized as follows. In Sec. II, we introduce the effective spin model with spatial anisotropy in the long-range interactions. In Sec. III, we describe the variational method for investigating the ground state of the model. In Sec. IV, we show the results for the phase diagram in a wide parameter space (Sec. IV A), the phase transitions driven by the anisotropy (Sec. IV B), and corresponding changes of the topological properties associated with the monopoles and antimonopoles as well as the emergent magnetic fields (Sec. IV C). Section V is devoted to the summary.

## II. MODEL

We consider an effective spin model for itinerant chiral magnets that includes long-range interactions arising from the spin-charge coupling and the spin-orbit coupling. The model was originally derived from the perturbation expansion for the Kondo lattice model with an antisymmetric spin-orbit coupling [7, 31]. The previous studies showed that this model exhibits VC and SkL in two dimensions [7, 8, 32] and HLs in three dimensions [31]. The Hamiltonian reads

$$\mathcal{H} = 2 \sum_{\eta} \left[ -J_{\eta} \mathbf{S}_{\mathbf{Q}_{\eta}} \cdot \mathbf{S}_{-\mathbf{Q}_{\eta}} + \frac{K_{\eta}}{N} (\mathbf{S}_{\mathbf{Q}_{\eta}} \cdot \mathbf{S}_{-\mathbf{Q}_{\eta}})^2 + i \mathbf{D}_{\eta} \cdot (\mathbf{S}_{\mathbf{Q}_{\eta}} \times \mathbf{S}_{-\mathbf{Q}_{\eta}}) \right]. \quad (1)$$

All the interactions are defined in terms of the Fourier component of spins,  $\mathbf{S}_{\mathbf{q}} = \frac{1}{\sqrt{N}} \sum_{\mathbf{l}} \mathbf{S}_{\mathbf{r}_l} e^{-i\mathbf{q} \cdot \mathbf{r}_l}$ , where  $\mathbf{S}_{\mathbf{r}_l}$  denotes the spin at a real-space position  $\mathbf{r}_l$  and  $N$  is the number of spins in the system. The sum in Eq. (1) is taken for a particular set of the wave vectors  $\mathbf{Q}_{\eta}$  derived from the electronic band structure in the original itinerant electron model (see below). We consider the model on a cubic lattice, following the previous study [31].

The first term in Eq. (1) represents the Ruderman-Kittel-Kasuya-Yosida (RKKY) interaction derived from the second-order perturbation with respect to the spin-charge coupling;  $J_{\eta} > 0$ . This prefers a helical magnetic order with wave vector  $\mathbf{Q}_{\eta}$ . The second term is the bi-quadratic interaction obtained from the fourth-order perturbation [7, 33]. The coupling constant  $K_{\eta}$  is positive, which favors a multiple- $Q$  state composed of a superposition of the helices with different  $\mathbf{Q}_{\eta}$ , such as VC, SkL, and HLs. The third term is a DM-type interaction originating from the second-order perturbation in terms of both spin-charge and antisymmetric spin-orbit couplings. Following the previous studies [7, 31], we set the directions of  $\mathbf{D}_{\eta}$  as  $\mathbf{D}_{\eta} \parallel \mathbf{Q}_{\eta}$ , namely,  $\mathbf{D}_{\eta} = D_{\eta} \mathbf{Q}_{\eta} / |\mathbf{Q}_{\eta}|$ . This term prefers a proper screw spin texture propagating in the direction of  $\mathbf{Q}_{\eta}$  with chirality depending on the sign of  $\mathbf{D}_{\eta} \cdot \mathbf{Q}_{\eta}$ .

In this Hamiltonian, all the interactions are specified

by the wave vectors  $\mathbf{Q}_\eta$ , which are set by multiple maxima in the spin-dependent bare susceptibility of itinerant electrons in the perturbation theory [7]. Following the previous study [31], we assume two types of  $\mathbf{Q}_\eta$ : One is a set of cubic wave vectors which are orthogonal to each other as  $\mathbf{Q}_1 = (Q, 0, 0)$ ,  $\mathbf{Q}_2 = (0, Q, 0)$ , and  $\mathbf{Q}_3 = (0, 0, Q)$  [see the inset of Fig. 1(d)], and the other is a set of tetrahedral wave vectors as  $\mathbf{Q}_1 = (Q, -Q, -Q)$ ,  $\mathbf{Q}_2 = (-Q, Q, -Q)$ ,  $\mathbf{Q}_3 = (-Q, -Q, Q)$ , and  $\mathbf{Q}_4 = (Q, Q, Q)$  [see the inset of Fig. 1(e)]. In the following analysis, we set  $Q = \pi/12$  without loss of generality.

To investigate the effects of spatial anisotropy, we introduce the anisotropy in the coupling constants  $J_\eta$ ,  $K_\eta$ , and  $D_\eta$  in Eq. (1). For the  $3Q$  case, we introduce the anisotropy along the [001] direction parallel to  $\mathbf{Q}_3$  as  $J_\eta = J$ ,  $D_\eta = D$ , and  $K_\eta = K$  for  $\eta = 1$  and  $2$ , and  $J_\eta = J'$ ,  $D_\eta = D'$ , and  $K_\eta = K'$  for  $\eta = 3$ . Meanwhile, for the  $4Q$  case, we introduce the anisotropy along the [111] direction parallel to  $\mathbf{Q}_4$  as  $J_\eta = J$ ,  $D_\eta = D$ , and  $K_\eta = K$  for  $\eta = 1, 2, 3$ , and  $J_\eta = J'$ ,  $D_\eta = D'$ , and  $K_\eta = K'$  for  $\eta = 4$ . In both cases, for simplicity, we assume the relations  $D'/D = J'/J$  and  $K'/K = (J'/J)^2$  considering the order of the perturbation expansion. Thus,  $J'/J > 1$  ( $< 1$ ) corresponds to the easy-axis (hard-axis) anisotropy along the [001] and [111] directions for the  $3Q$  and  $4Q$  cases, respectively.

### III. METHOD

We study the ground state of the model in Eq. (1) by a variational method. The method is an extension of that used in the previous study [31] to the anisotropic cases. We consider the following three types of spin textures as the variational states. The first one is a superposition of sinusoidal waves given by

$$\mathbf{S}_{\mathbf{r}_l} \propto \sum_{\eta=1}^n a_\eta \mathbf{e}_\eta^0 \cos \mathcal{Q}_{\eta l}, \quad (2)$$

where  $\mathbf{e}_\eta^0$  is the unit vector parallel to  $\mathbf{Q}_\eta$  and  $\mathcal{Q}_{\eta l} = \mathbf{Q}_\eta \cdot \mathbf{r}_l + \phi_\eta$ ;  $n = 3$  and  $4$  for the  $3Q$  and  $4Q$  cases, respectively.  $a_\eta$  and  $\phi_\eta$  denote the amplitude and phase of the  $\mathbf{Q}_\eta$  component, respectively. As this is the nonchiral state which has no energy gain from the DM-type interaction, we call it the  $mQ$  nonchiral state ( $mQ$ -NC), where  $m = 1, 2, \dots$ ,  $n$  is the number of the components with nonzero  $a_\eta$  in Eq. (2). The second variational state is given by

$$\mathbf{S}_{\mathbf{r}_l} \propto \sum_{\eta=1}^n a_\eta (\mathbf{e}_\eta^1 \cos \mathcal{Q}_{\eta l} + \mathbf{e}_\eta^2 \sin \mathcal{Q}_{\eta l}), \quad (3)$$

where  $\mathbf{e}_\eta^1$  and  $\mathbf{e}_\eta^2$  are the unit vectors which satisfy  $\mathbf{e}_\eta^1 \times \mathbf{e}_\eta^2 = \mathbf{e}_\eta^0$ ;  $n = 3$  and  $4$  for the  $3Q$  and  $4Q$  cases, respectively, as in Eq. (2). Here, we set  $\mathbf{e}_1^1 = \hat{y}$ ,  $\mathbf{e}_2^1 = \hat{z}$ , and  $\mathbf{e}_3^1 = \hat{x}$  for the  $3Q$  case, and  $\mathbf{e}_\eta^1 = \hat{z} \times \mathbf{e}_\eta^0 / |\hat{z} \times \mathbf{e}_\eta^0|$  for the  $4Q$  case, where  $\hat{x}$ ,  $\hat{y}$ , and  $\hat{z}$  are the unit vectors in the  $xyz$  coordinates. This is a chiral multiple- $Q$  state,

which has an energy gain from the DM-type interaction in contrast to the nonchiral one in Eq. (2). We call it the  $1Q$  helical state ( $1Q$ -H) when only one of  $a_\eta$  is nonzero, while the  $2Q$  vortex crystal ( $2Q$ -VC) when two of them are nonzero. Meanwhile, for the states with more than two nonzero components, we have topologically different states depending on the existence of hedgehogs and antihedgehogs (see below); we call the states with hedgehogs and antihedgehogs the  $3Q$  and  $4Q$  hedgehog lattices ( $3Q$ - and  $4Q$ -HLs), while otherwise simply the  $3Q$  and  $4Q$  states. The third variational state is called the double- $Q$  chiral stripe ( $2Q$ -CS) found in the previous study [34], which is given by

$$\mathbf{S}_{\mathbf{r}_l} \propto \sqrt{1 - u_{\eta'l}^2} (\mathbf{e}_\eta^1 \cos \mathcal{Q}_{\eta l} + \mathbf{e}_\eta^2 \sin \mathcal{Q}_{\eta l}) + u_{\eta'l} \mathbf{e}_\eta^0, \quad (4)$$

where  $u_{\eta'l} = v \sin \mathcal{Q}_{\eta'l}$ ;  $v$  denotes the amplitude of the sinusoidal wave, and  $\eta$  and  $\eta'$  take two of three and four components in the  $3Q$  and  $4Q$  cases, respectively.

In the variational calculations,  $a_\eta$ ,  $\phi_\eta$ , and  $v$  are treated as variational parameters that are optimized to find the lowest-energy state.  $a_\eta$  and  $v$  are varied from 0 to 1, while  $\phi_\eta$  from 0 to  $Q$  for the  $3Q$  case and 0 to  $2\pi$  for the  $4Q$  case. We prepare each variational state with the normalization of the spin length at every site as  $|\mathbf{S}_{\mathbf{r}_l}| = 1$ , optimize the energy with respect to the variational parameters, and then compare the energies among different variational states. Note that the optimized energy is unchanged by exchanging  $\eta$  and  $\eta'$ , except for the  $2Q$ -CS state including the helix running along the anisotropic axis in  $\eta$  or  $\eta'$ . In the following analysis, we impose the following constraints on the variational parameters  $a_\eta$  from the symmetry point of view:  $a_1 = a_2$  for all the multiple- $Q$  states in the  $3Q$  case, and  $a_1 = a_2$  (or equivalently,  $a_2 = a_3$  or  $a_3 = a_1$ ) for the  $2Q$ -NC and VC in the  $4Q$  case. In addition, we set  $a_1 = a_2 = a_3$  for all the  $3Q$  and  $4Q$  states including the HLs for the  $4Q$  case. In all cases,  $\sum_\eta a_\eta^2 = 1$ . We perform the variational calculations on the cubic lattice with  $N = 24^3$  sites under the periodic boundary conditions in all three directions. Note that there is no finite-size effects as  $Q = \pi/12$  induces magnetic orders with period of 24.

For the optimized states, we calculate the magnetic moment with wave vector  $\mathbf{Q}_\eta$  [35],

$$m_{\mathbf{Q}_\eta} = \sqrt{\frac{S(\mathbf{Q}_\eta) + S(-\mathbf{Q}_\eta)}{N}}, \quad (5)$$

where  $S(\mathbf{q})$  is the spin structure factor defined by

$$S(\mathbf{q}) = \frac{1}{N} \sum_{l,l'} \mathbf{S}_{\mathbf{r}_l} \cdot \mathbf{S}_{\mathbf{r}_{l'}} e^{-i\mathbf{q} \cdot (\mathbf{r}_l - \mathbf{r}_{l'})}. \quad (6)$$

We also calculate a topological quantity called the monopole charge, which is defined for each unit cube composed of the neighboring eight sites on the cubic lattice as [27, 31]

$$Q_m(\mathbf{R}_j) = \frac{1}{4\pi} \sum_{p \in \text{jth unit cube}} \Omega_p, \quad (7)$$

where  $\mathbf{R}_j$  is the center position of  $j$ th unit cube and  $\Omega_p$  is the solid angle spanned by four spins on the  $p$ th square plaquette surrounding the unit cube ( $p = 1, 2, \dots, 6$ ).  $\Omega_p$  is calculated by dividing the plaquette into two triangles  $\Delta_i$  ( $i = 1, 2$ ) and taking the sum of the solid angles of three spins in the triangles as  $\Omega_p = \Omega_{\Delta_1} + \Omega_{\Delta_2}$ , where

$$\Omega_{\Delta_i} = 2 \tan^{-1} \left[ \frac{\mathbf{S}_1 \cdot (\mathbf{S}_2 \times \mathbf{S}_3)}{1 + \mathbf{S}_1 \cdot \mathbf{S}_2 + \mathbf{S}_2 \cdot \mathbf{S}_3 + \mathbf{S}_3 \cdot \mathbf{S}_1} \right]. \quad (8)$$

Here,  $\mathbf{S}_1$ ,  $\mathbf{S}_2$ , and  $\mathbf{S}_3$  are three spins on the triangle  $\Delta_i$  in the clockwise order viewed from the center of the cube. The argument in  $\tan^{-1}$  is taken in the range of  $[-\pi, \pi]$ . The monopole charge in Eq. (7) signals the position of hedgehogs and antihedgehogs by  $Q_m(\mathbf{R}_j) = +1$  and  $-1$ , respectively. We also compute the total number of hedgehogs and antihedgehogs in the magnetic unit cell by

$$N_m = \sum_{j \in \text{magnetic unit cell}} |Q_m(\mathbf{R}_j)|. \quad (9)$$

We also calculate the scalar spin chirality which gives the emergent magnetic field through the Berry phase. We compute  $\chi_{\mathbf{r}_i} = (\chi_{\mathbf{r}_i}^x, \chi_{\mathbf{r}_i}^y, \chi_{\mathbf{r}_i}^z)$  at each site, whose component is defined by the summation of the spin triple products on the adjacent four triangles as [27, 31]

$$\chi_{\mathbf{r}_i}^\alpha = \frac{1}{8} \sum_{\beta\gamma\nu\beta\nu\gamma} \varepsilon^{\alpha\beta\gamma} \nu_\beta \nu_\gamma \mathbf{S}_{\mathbf{r}_i} \cdot (\mathbf{S}_{\mathbf{r}_i+\nu_\beta \mathbf{e}_\beta} \times \mathbf{S}_{\mathbf{r}_i+\nu_\gamma \mathbf{e}_\gamma}). \quad (10)$$

Here,  $\beta$  and  $\gamma$  are the directions perpendicular to  $\alpha$ , and  $\nu_{\beta(\gamma)} = \pm 1$ .

The definitions in Eqs. (7), (8), and (10) indicate that the hedgehogs and antihedgehogs are regarded as magnetic monopoles and antimonopoles that are the sources and sinks of the emergent magnetic field, respectively. Real-space mapping of the positions of the monopoles and antimonopoles with  $\chi_{\mathbf{r}_i}$  manifests the flow of the emergent magnetic field; see Sec. IV C.

## IV. RESULTS

In this section, we show the results obtained by the variational calculations for the model in Eq. (1). In Sec. IV A, we show the phase diagrams on the  $D(D')$ - $K(K')$  plane while changing the anisotropy. Next, in Sec. IV B, we show how the magnetic and topological properties change through the phase transitions caused by changing the anisotropy. Finally, in Sec. IV C, we show real-space distributions of hedgehogs and antihedgehogs, and the flow of the scalar spin chirality  $\chi_{\mathbf{r}_i}$ .

### A. Phase diagram

First, we show the phase diagrams obtained by the variational calculations for the 3Q case in Figs. 2(a)-2(c)

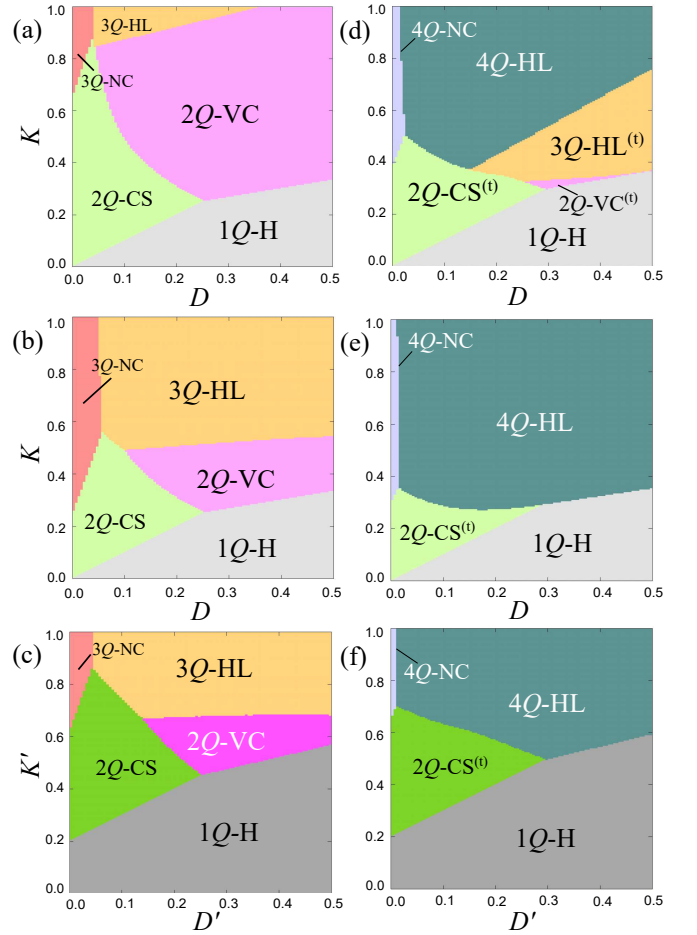


FIG. 2. Phase diagrams of the model in Eq. (1) obtained by the variational calculations for (a)-(c) the 3Q case and (d)-(f) the 4Q case: (a),(d)  $J'/J = 0.8$  (hard-axis), (b),(e)  $J'/J = 1.0$  (isotropic), and (c),(f)  $J'/J = 0.8$  (easy-axis). 1Q-H, 2Q-VC, 2Q-CS, 3Q(4Q)-HL, and 3Q(4Q)-NC represent the 1Q helical, the 2Q vortex crystal, the 2Q chiral stripe, the 3Q(4Q) hedgehog lattice, and the 3Q(4Q) nonchiral states, respectively. The light and dark colors for 2Q-VC and 1Q-H denote the differences in the constituent wave vectors.

and for the 4Q case in Figs. 2(d)-2(f): (a) and (d) are for the hard-axis anisotropy with  $J'/J = 0.8$ , (b) and (e) are for the isotropic cases with  $J'/J = 1.0$ , and (c) and (f) are for the easy-axis anisotropy with  $J'/J = 0.8$ . We plot the results for  $D$  and  $K$  when  $J'/J \leq 1.0$ , while for  $D'$  and  $K'$  when  $J'/J > 1.0$ , with the relations  $D'/D = J'/J$  and  $K'/K = (J'/J)^2$ . Note that the 2Q-NC, VC, CS, and 3Q-HL are different states between the 3Q and 4Q cases due to the different sets of  $\mathbf{Q}_\eta$ .

The results for the isotropic cases in Figs. 2(b) and 2(e) agree with those in the previous study [31]; the 3Q- and 4Q-HLs appear in a wide range of  $D$  and  $K$ , indicating that both spin-orbit and spin-charge couplings play an important role in the stabilization of the HLs. When we introduce the hard-axis anisotropy, as shown in Figs. 2(a) and 2(d), the regions of these HLs are shrunk, and instead, the 2Q-VC and CS (the 2Q-CS and the 3Q-HL)

are extended for the 3Q (4Q) case; in the 3Q case, the 2Q-VC and CS states are composed of  $\mathbf{Q}_1$  and  $\mathbf{Q}_2$ , while in the 4Q case, the 2Q-CS is composed of two out of  $\mathbf{Q}_1$ ,  $\mathbf{Q}_2$ , and  $\mathbf{Q}_3$ , and the 3Q-HL is of  $\mathbf{Q}_1$ ,  $\mathbf{Q}_2$ , and  $\mathbf{Q}_3$ . On the other hand, when we introduce the easy-axis anisotropy, as shown in Figs. 2(c) and 2(f), the 1Q-H is extended to the regions of the HLs, which is composed of  $\mathbf{Q}_3$  ( $\mathbf{Q}_4$ ) in the 3Q (4Q) case. These results are understood from the fact that the hard(easy)-axis anisotropy tends to destabilize (stabilize) the helix propagating along  $\mathbf{Q}_3 \parallel [001]$  and  $\mathbf{Q}_4 \parallel [111]$  for the 3Q and 4Q cases, respectively.

### B. Phase transitions driven by anisotropy

The results in Fig. 2 indicate that the system exhibits phase transitions from the isotropic HLs to other magnetic states by introducing the anisotropy. We discuss such phase transitions in detail, for  $D = 0.3$  and  $K = 0.8$  where the 3Q- and 4Q-HLs are stable in the isotropic 3Q and 4Q cases, respectively. Figures 3(a) and 3(b) show the results for the 3Q and 4Q cases, respectively: anisotropy dependences of the optimized energy per site,  $E$ , the variational parameters  $a_3$  and  $a_4$ , the magnetic moments  $m_{\mathbf{Q}_\eta}$ , and the total number of hedgehogs and antihedgehogs in the magnetic unit cell,  $N_m$ .

Let us first discuss the 3Q case in Fig. 3(a). In this case, we identify five different phases from the energy comparison and the topological nature. The energy comparison is plotted in the upper panel of Fig. 3(a) for the 1Q-H state with  $a_3 = 1$  (gray), 2Q-VC with  $a_3 = 0$  (light pink), 2Q-VC with  $a_1 = 0$  (or  $a_2 = 0$ ) (dark pink), and 3Q (orange). The values of  $a_3$  and  $m_{\mathbf{Q}_\eta}$  for the lowest-energy state are shown in the middle and lower panels. In the region where the 3Q variational state has the lowest energy, we distinguish two topologically different phases by  $N_m$  plotted in the lower panel. We describe the details below.

In the isotropic case, the system exhibits the 3Q-HL with the same amplitude as indicated by  $a_3 = 1/\sqrt{3}$  ( $= a_1 = a_2$ ) and  $m_{\mathbf{Q}_1} = m_{\mathbf{Q}_2} = m_{\mathbf{Q}_3}$  as plotted in the middle and lower panels of Fig. 3(a), respectively. This state is topologically nontrivial as it includes four pairs of hedgehogs and antihedgehogs in the magnetic unit cell, i.e.,  $N_m = 8$ , as plotted in the lower panel of Fig. 3(a). We find that the phases of the three ordering vectors are  $\phi_1 = \phi_2 = \phi_3 = Q/2$ , which indicates that the hedgehogs and antihedgehogs are located at the centers of the cubes so as to avoid the lattice sites [31].

When we introduce the hard-axis anisotropy by taking  $J'/J < 1$ , the 3Q-HL remains stable down to  $J'/J \simeq 0.8875$  while the spin texture is modulated by reflecting the anisotropy as  $a_3 < 1/\sqrt{3}$  ( $a_1 = a_2 > 1/\sqrt{3}$ ) and  $m_{\mathbf{Q}_1} = m_{\mathbf{Q}_2} > m_{\mathbf{Q}_3}$ . In the anisotropic HL,  $\phi_\eta$  takes 0 or  $Q/2$ , which is chosen so as to locate the hedgehogs and antihedgehogs at the interstitial positions appropriately. For  $J'/J \lesssim 0.8875$ , the 3Q-HL is taken over by the 2Q-VC with  $a_3 = 0$  ( $a_1 = a_2 = 1/\sqrt{2}$ ) and  $m_{\mathbf{Q}_3} = 0$ , as

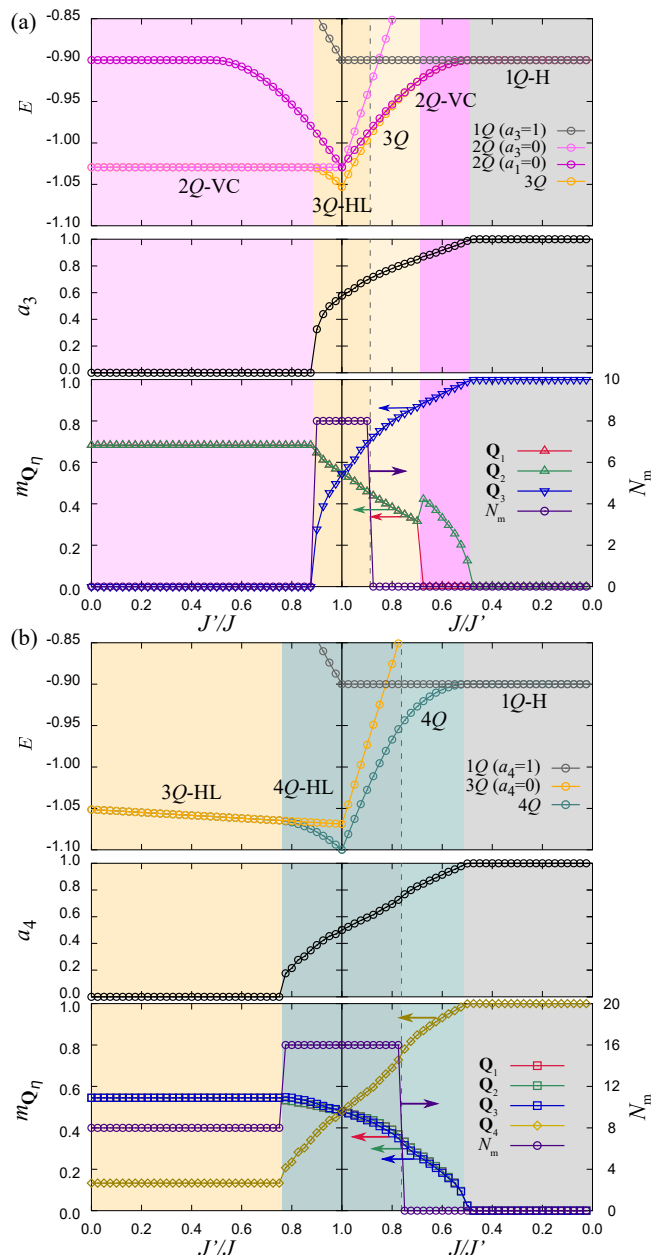


FIG. 3. Anisotropy dependences of the variational energy per site,  $E$ , the amplitude of the helix in the  $J'$  direction,  $a_3$  or  $a_4$ , the magnetic moment with the wave vector  $\mathbf{Q}_\eta$ ,  $m_{\mathbf{Q}_\eta}$ , and the number of hedgehog and antihedgehog,  $N_m$ , for the (a) 3Q and (b) 4Q cases. The dashed lines represent the topological transitions with the changes of  $N_m$ . The results are calculated for  $D = 0.3$  and  $K = 0.8$  in Eq. (1). We take  $J(J')$  as the energy unit for  $J'/J < 1$  ( $> 1$ ).

shown in the left hand side of Fig. 3(a). In this state, both  $\phi_1$  and  $\phi_2$  are optimized to be  $Q/2$  so that the vortex and antivortex cores are located at the centers of the square plaquettes. At this phase transition,  $N_m$  changes from 8 to 0, as shown in the lower panel of Fig. 3(a). Thus, the results indicate that the transition occurs from the topologically nontrivial 3Q-HL to the topologically trivial

2Q-VC by the hard-axis anisotropy.

On the other hand, when we introduce the easy-axis anisotropy as  $J'/J > 1$ , the system shows more complicated multiple phase transitions, as shown in the right hand side of Fig. 3(a). Note that the right hand side is plotted for  $J/J'$  instead of  $J'/J$  to cover all the parameter range to the limit of  $J'/J \rightarrow \infty$ . The 3Q-HL with  $N_m = 8$  is stable up to  $J/J' \simeq 0.8875$  while the spin configuration is modulated as  $a_3 > a_1 = a_2$  and  $m_{\mathbf{Q}_3} > m_{\mathbf{Q}_1} = m_{\mathbf{Q}_2}$ . At  $J/J' \simeq 0.8875$ , the topologically nontrivial 3Q-HL changes into the topologically trivial 3Q state with  $N_m = 0$ . We note that  $\phi_\eta$  takes 0 or  $Q/2$  for  $J/J' \gtrsim 0.7875$  similar to those for  $0.8875 \lesssim J'/J < 1$ , whereas  $\phi_1 = \phi_2 = \phi_3 = 0$  for  $J/J' \lesssim 0.7875$ ; the origin of the phase shifts is unclear, while in both regions, the hedgehogs and antihedgehogs are located at the interstitial positions. With a further decrease of  $J/J'$  to  $\simeq 0.6875$ , the 3Q state is taken over by the 2Q-VC with  $a_1 = 0$  and  $a_3 > a_2 > 0$ , and  $m_{\mathbf{Q}_1} = 0$  and  $m_{\mathbf{Q}_3} > m_{\mathbf{Q}_2} > 0$ , as shown in the middle and lower panels of Fig. 3(a). This state is different from the 2Q-VC stable for  $J'/J \lesssim 0.8875$ ; it has no singular points where the spin length vanishes since it is composed of two helices with different amplitude. We note that  $\phi_\eta$  varies with  $J'/J$  in this state. Finally, for  $J/J' \lesssim 0.4875$ , the 2Q-VC is replaced by the 1Q-H with  $a_3 = 1$  and  $a_1 = a_2 = 0$ , and  $m_{\mathbf{Q}_3} = 1$  and  $m_{\mathbf{Q}_1} = m_{\mathbf{Q}_2} = 0$ , which is stable to the easy-axis limit,  $J/J' \rightarrow 0$ .

Next, we discuss the 4Q case in Fig. 3(b). In this case, we identify four phases. The energy comparison is plotted in the top panel of Fig. 3(b) for 1Q-H with  $a_4 = 1$  (gray), 3Q with  $a_4 = 0$  (orange), and 4Q (green). As in the 3Q case above, we obtain two topologically different phases in the 4Q region from the values of  $N_m$  plotted in the lower panel of Fig. 3(b), as described below.

In the isotropic case, the system exhibits the 4Q-HL with equal amplitude of the four helices, i.e.,  $a_4 = 1/2$  ( $= a_1 = a_2 = a_3$ ) and  $m_{\mathbf{Q}_1} = m_{\mathbf{Q}_2} = m_{\mathbf{Q}_3} = m_{\mathbf{Q}_4}$ . This state is topologically nontrivial as it includes eight pairs of hedgehogs and antihedgehogs, i.e.,  $N_m = 16$ , as shown in the lower panel of Fig. 3(b). We find that  $\phi_\eta$  satisfy the relation  $\sum_{\eta=1}^4 \phi_\eta = (2k+1)\pi$  ( $k$  is an integer) to place the hedgehogs and antihedgehogs at the centers of the cubes [31]. When we introduce the hard-axis anisotropy by taking  $J'/J < 1$ , the 4Q-HL remains stable down to  $J'/J \simeq 0.7625$ , while the spin texture is modulated as  $a_4 < 1/2$  ( $a_1 = a_2 = a_3 > 1/2$ ) and  $0 < m_{\mathbf{Q}_4} < m_{\mathbf{Q}_1} = m_{\mathbf{Q}_2} = m_{\mathbf{Q}_3}$ . For  $J'/J \lesssim 0.7625$ , the 4Q-HL is taken over by the 3Q-HL with  $a_1 = a_2 = a_3 = 1/\sqrt{3}$ ,  $a_4 = 0$ , and  $m_{\mathbf{Q}_1} = m_{\mathbf{Q}_2} = m_{\mathbf{Q}_3} > m_{\mathbf{Q}_4}$ , as shown in the left hand side of Fig. 3(b). The nonzero small value of  $m_{\mathbf{Q}_4}$  despite  $a_4 = 0$  is a consequence of the normalization of the spin length (see Sec. III). In this state,  $\phi_\eta$  are optimized as  $\phi_1 = \phi_2 = \phi_3 = Q/2$ . At this phase transition,  $N_m$  changes from 16 to 8. Note that the magnetic unit cell of the 3Q-HL becomes four times smaller than that of the 4Q-HL; it is rhombohedral since the three ordering wave vectors,  $\mathbf{Q}_1$ ,  $\mathbf{Q}_2$ , and  $\mathbf{Q}_3$ , are not orthogonal to each

other.

On the other hand, when we introduce the easy-axis anisotropy by  $J'/J > 1$ , the system shows two phase transitions as shown in the right hand side of Fig. 3(b). The 4Q-HL is stable up to  $J/J' \simeq 0.7625$ , while the spin configuration is modulated reflecting the easy-axis anisotropy as  $a_1 = a_2 = a_3 < 1/2 < a_4$ , and  $m_{\mathbf{Q}_1} = m_{\mathbf{Q}_2} = m_{\mathbf{Q}_3} < m_{\mathbf{Q}_4}$ . At  $J/J' \simeq 0.7625$ , the topologically nontrivial 4Q-HL with  $N_m = 16$  is replaced by the topologically trivial 4Q state with  $N_m = 0$ , as shown in the lower panel of Fig. 3(b). In these anisotropic 4Q-HL and 4Q states, the values of  $\phi_\eta$  depend on  $J'/J$ , but the sum always satisfies  $\sum_{\eta=1}^4 \phi_\eta = (2k+1)\pi$ , as for the isotropic 4Q-HL. While further decreasing  $J/J'$ , the 4Q state is taken over by the 1Q-H with  $a_1 = a_2 = a_3 = 0$  and  $a_4 = 1$ , and  $m_{\mathbf{Q}_1} = m_{\mathbf{Q}_2} = m_{\mathbf{Q}_3} = 0$  and  $m_{\mathbf{Q}_4} = 1$  for  $J/J' \lesssim 0.5125$ .

### C. Topological properties

In the previous section, we found multiple phase transitions by changing the anisotropy  $J'/J$ , including the topological ones accompanied by the changes of  $N_m$ . In this section, we discuss the topological aspects in detail, by tracing the real-space positions of the monopoles and antimonopoles corresponding to the hedgehogs and antihedgehogs, respectively, as well as the emergent magnetic field from the noncoplanar spin configurations.

Figures 4 and 5 display the real-space pictures of the monopoles and antimonopoles (magenta and cyan balls) for the 3Q and 4Q cases, respectively. The positions are determined by calculating the monopole charge in Eq. (7). We also plot  $\chi_{\mathbf{r}_l}$  in Eq. (10) by arrows to show the flow of the emergent magnetic field. For better visibility, we display the arrows whose norm is larger than a certain threshold in each case.

First, we discuss the 3Q case in Fig. 4. In the 2Q-VC under the hard-axis anisotropy, although there are no monopoles and antimonopoles, weak but nonzero  $\chi_{\mathbf{r}_l}$  appears locally around the antivortex cores, as exemplified in Fig. 4(a) for  $J'/J = 0.875$ .  $\chi_{\mathbf{r}_l}$  are all parallel to the [001] direction, while they form staggered flow around each core. While increasing  $J'/J$  above  $\simeq 0.875$ , the system undergoes a phase transition from the 2Q-VC to the 3Q-HL. At this phase transition, monopoles and antimonopoles are created in pair from the flows of  $\chi_{\mathbf{r}_l}$ , and accordingly, the flows change qualitatively;  $\chi_{\mathbf{r}_l}$  starts to flow from the monopoles (sources) to the antimonopoles (sinks), as shown in Fig. 4(b). While further increasing  $J'/J$ , the monopoles and antimonopoles change their relative positions with keeping their  $z$  coordinates, and for the isotropic case with  $J'/J = 1.0$  shown in Fig. 4(c), they form spiral structures in all the  $x$ ,  $y$ , and  $z$  directions [26, 31]. When we introduce weak easy-axis anisotropy, the monopoles and antimonopoles move again with keeping the  $z$  coordinates and approach each other as shown in Fig. 4(d), and eventually annihilate

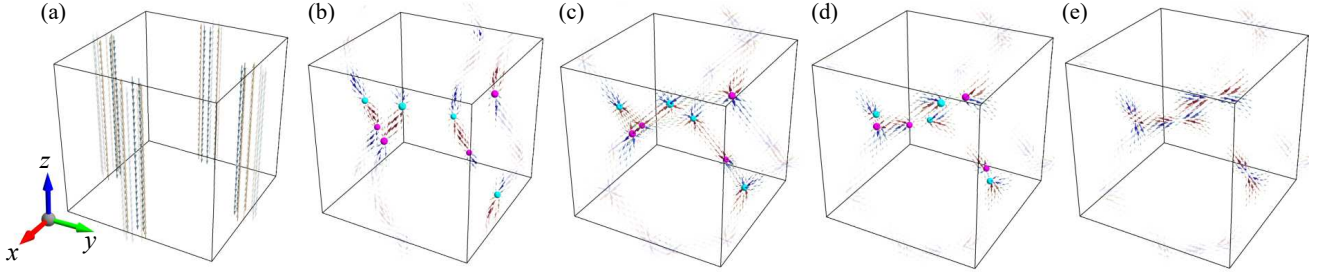


FIG. 4. Real-space configurations of the scalar spin chirality  $\chi_{\mathbf{r}_l}$  (arrows), and the monopoles and antimonopoles (magenta and cyan balls, respectively) in a magnetic unit cell obtained from the variational calculations for the  $3Q$  case: (a)  $J'/J = 0.875$ , (b)  $J'/J = 0.9$ , (c)  $J'/J = 1.0$ , (d)  $J'/J = 0.9$ , and (e)  $J'/J = 0.875$ .  $\chi_{\mathbf{r}_l}$  are plotted when their lengths are longer than a certain threshold for better visibility. The color of the arrows represents the  $z$  component of  $\chi_{\mathbf{r}_l}$ ; pale color is used for the arrows in the neighboring magnetic unit cells.

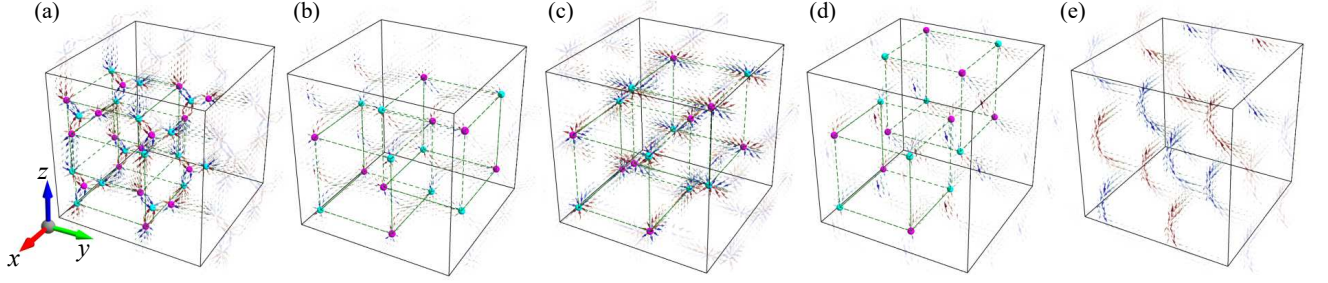


FIG. 5. Similar plots for the  $4Q$  case: (a)  $J'/J = 0.75$ , (b)  $J'/J = 0.775$ , (c)  $J'/J = 1.0$ , (d)  $J'/J = 0.775$ , and (e)  $J'/J = 0.75$ . The notations are common to those in Fig. 4. Note that the magnetic unit cell is one fourth of the whole cube in (a). The green dashed cubes are the guides for eyes; see the text for details.

in pair at the transition to the  $3Q$  state at  $J'/J \simeq 0.9$ . Even in this topologically trivial state with no monopoles and antimonopoles, there remains nonzero flow of  $\chi_{\mathbf{r}_l}$ , especially near the pair annihilation points, as shown in Fig. 4(e) for  $J'/J = 0.875$ .

Next, we discuss the  $4Q$  case in Fig. 5. In the  $3Q$ -HL state under the hard-axis anisotropy, there are four pairs of monopoles and antimonopoles in the magnetic unit cell, as exemplified in Fig. 5(a) for  $J'/J = 0.75$ . Note that the volume of the magnetic unit cell is four times smaller than the whole cube in Fig. 5(a), as mentioned above.  $\chi_{\mathbf{r}_l}$  distribute to interconnect the monopoles and antimonopoles. While increasing  $J'/J$  above  $\simeq 0.75$ , the system undergoes a phase transition from the  $3Q$ -HL to the  $4Q$ -HL. At this phase transition, monopoles and antimonopoles connected by the green dotted lines in Fig. 5(a) remain and the others disappear. The remaining ones change their relative positions with keeping the sizes and shapes of the two green cubes, as exemplified in Fig. 5(b) for  $J'/J = 0.775$ . While further increasing  $J'/J$ , the monopoles and antimonopoles come to form the body-centered-cubic lattice for the isotropic case with  $J'/J = 1.0$  shown in Fig. 5(c). When we introduce weak easy-axis anisotropy, the monopoles of one cube and antimonopoles of the other cube approach each other, and  $\chi_{\mathbf{r}_l}$  becomes relatively strong between them, as shown in Fig. 5(d) for  $J'/J = 0.775$ . By further decreasing  $J'/J$ ,

the system undergoes the phase transition from the  $4Q$ -HL to the  $4Q$  state caused by the pair annihilation of the remaining monopoles and antimonopoles. Similar to the  $3Q$  state in Fig. 4(e), even after the monopoles and antimonopoles vanish, nonzero flow of  $\chi_{\mathbf{r}_l}$  remains near the pair annihilation points, as exemplified in Fig. 5(e) for  $J'/J = 0.75$ .

## V. SUMMARY

In conclusion, we have theoretically investigated the control of the spin textures and their topological properties by changing the spatial anisotropy in the long-range interactions generated by the itinerant nature of electrons. We showed that the two types of the three-dimensional HLs, which are stable in the spatially isotropic cases, change their dimensionality and topology for the hard- and easy-axis anisotropy along one of the helical directions. In the case of the HL composed of three orthogonal helices ( $3Q$ -HL), we found that the HL is changed into a two-dimensional vortex crystal ( $2Q$ -VC) for the hard-axis anisotropy, while into a topologically nontrivial  $3Q$  state, another  $2Q$ -VC, and finally, a one-dimensional helix ( $1Q$ -H) as increasing the easy-axis anisotropy. On the other hand, in the case of the HL composed of four tetrahedral helices ( $4Q$ -HL), we found that

the HL turns into a  $3Q$ -HL for the hard-axis anisotropy, while into a topologically trivial  $4Q$  state and a  $1Q$ -H as increasing the easy-axis anisotropy. We showed that the transitions between the topologically nontrivial and trivial states are characterized by pair annihilation of the monopoles and antimonopoles. Furthermore, we clarified the systematic changes of the topological properties of these spin textures, focusing on the real-space positions of the monopoles and antimonopoles, and the flows of the emergent magnetic field defined by the scalar spin chirality. Our results indicate that the spatial anisotropy in chiral magnets drives not only the magnetic phase transitions with dimensional reduction but also the topological properties from the Berry phase mechanism.

Experimentally, two types of the HLs as well as SkL are realized in  $\text{MnSi}_{1-x}\text{Ge}_x$  [13, 19]. Although the microscopic origin is under debate, a scenario was proposed based on the itinerant nature of electrons included in the present model in Eq. (1) with isotropic interactions [31]. In this model, the anisotropy would be introduced through the change of the electronic state of itinerant electrons, and hence, our results suggest that the

interesting transitions found above might be caused, e.g., by external pressure and chemical substitution, which modifies the electronic band structure. Such experimental studies as well as further sophisticated theories based on realistic model parameters are left for future work.

## ACKNOWLEDGMENTS

This research was supported by Grant-in-Aid for Scientific Research Grants Numbers JP18K03447, JP19H05822 and JP19H05825, and JST CREST (JPMJCR18T2), and the Chirality Research Center in Hiroshima University and JSPS Core-to-Core Program, Advanced Research Networks. K.S. was supported by the Program for Leading Graduate Schools (MERIT-WINGS). S.O. was supported by JSPS through the research fellowship for young scientists. Parts of the numerical calculations were performed in the supercomputing systems in ISSP, the University of Tokyo.

- 
- [1] I. Dzyaloshinsky, *J. Phys. Chem. Solids* **4**, 241 (1958).  
 [2] T. Moriya, *Phys. Rev.* **120**, 91 (1960).  
 [3] A. Yoshimori, *J. Phys. Soc. Japan* **14**, 807 (1959).  
 [4] T. Moriya, *Solid State Commun.* **20**, 291 (1976).  
 [5] G. Shirane, R. Cowley, C. Majkrzak, J. B. Sokoloff, B. Pagonis, C. H. Perry, and Y. Ishikawa, *Phys. Rev. B* **28**, 6251 (1983).  
 [6] M. Uchida, Y. Onose, Y. Matsui, and Y. Tokura, *Science* **311**, 359 (2006).  
 [7] S. Hayami, R. Ozawa, and Y. Motome, *Phys. Rev. B* **95**, 224424 (2017).  
 [8] S. Hayami and Y. Motome, *Phys. Rev. Lett.* **121**, 137202 (2018).  
 [9] N. D. Khanh, T. Nakajima, X. Yu, S. Gao, K. Shibata, M. Hirschberger, Y. Yamasaki, H. Sagayama, H. Nakao, L. Peng, K. Nakajima, R. Takagi, T. Arima, Y. Tokura, and S. Seki, *Nat. Nanotechnol.* **15**, 444 (2020).  
 [10] S. Mühlbauer, B. Binz, F. Jonietz, C. Pfleiderer, A. Rosch, A. Neubauer, R. Georgii, and P. Böni, *Science* **323**, 915 (2009).  
 [11] X. Z. Yu, Y. Onose, N. Kanazawa, J. H. Park, J. H. Han, Y. Matsui, N. Nagaosa, and Y. Tokura, *Nature* **465**, 901 (2010).  
 [12] A. Tonomura, X. Yu, K. Yanagisawa, T. Matsuda, Y. Onose, N. Kanazawa, H. S. Park, and Y. Tokura, *Nano Lett.* **12**, 1673 (2012).  
 [13] Y. Fujishiro, N. Kanazawa, T. Nakajima, X. Z. Yu, K. Ohishi, Y. Kawamura, K. Kakurai, T. Arima, H. Mitamura, A. Miyake, K. Akiba, M. Tokunaga, A. Matsumoto, K. Kindo, T. Koretsune, R. Arita, and Y. Tokura, *Nat. Commun.* **10**, 1059 (2019).  
 [14] Y. Fujishiro, N. Kanazawa, and Y. Tokura, *Appl. Phys. Lett.* **116**, 090501 (2020).  
 [15] X. Yu, N. Kanazawa, Y. Onose, K. Kimoto, W. Zhang, S. Ishiwata, Y. Matsui, and Y. Tokura, *Nat. Mater.* **10**, 106 (2011).  
 [16] W. Münzer, A. Neubauer, T. Adams, S. Mühlbauer, C. Franz, F. Jonietz, R. Georgii, P. Böni, B. Pedersen, M. Schmidt, A. Rosch, and C. Pfleiderer, *Phys. Rev. B* **81**, 041203(R) (2010).  
 [17] S. Seki, X. Z. Yu, S. Ishiwata, and Y. Tokura, *Science* **336**, 198 (2012).  
 [18] T. Adams, A. Chacon, M. Wagner, A. Bauer, G. Brandl, B. Pedersen, H. Berger, P. Lemmens, and C. Pfleiderer, *Phys. Rev. Lett.* **108**, 237204 (2012).  
 [19] Y. Tokunaga, X. Z. Yu, J. S. White, H. M. Rønnow, D. Morikawa, Y. Taguchi, and Y. Tokura, *Nat. Commun.* **6**, 7638 (2015).  
 [20] T. Tanigaki, K. Shibata, N. Kanazawa, X. Yu, Y. Onose, H. S. Park, D. Shindo, and Y. Tokura, *Nano Lett.* **15**, 5438 (2015).  
 [21] S. Ishiwata, T. Nakajima, J.-H. Kim, D. S. Inosov, N. Kanazawa, J. S. White, J. L. Gavilano, R. Georgii, K. M. Seemann, G. Brandl, P. Manuel, D. D. Khalyavin, S. Seki, Y. Tokunaga, M. Kinoshita, Y. W. Long, Y. Kaneko, Y. Taguchi, T. Arima, B. Keimer, and Y. Tokura, *Phys. Rev. B* **101**, 134406 (2020).  
 [22] M. V. Berry, *Proc. R. Soc. Lond. A* **392**, 45 (1984).  
 [23] D. Xiao, M.-C. Chang, and Q. Niu, *Rev. Mod. Phys.* **82**, 1959 (2010).  
 [24] N. Nagaosa and Y. Tokura, *Nat. Nanotechnol.* **8**, 899 (2013).  
 [25] G. E. Volovik, *J. Phys. C Solid State Phys.* **20**, L83 (1987).  
 [26] N. Kanazawa, Y. Nii, X.-X. Zhang, A. Mishchenko, G. De Filippis, F. Kagawa, Y. Iwasa, N. Nagaosa, and Y. Tokura, *Nat. Commun.* **7**, 11622 (2016).  
 [27] S. Okumura, S. Hayami, Y. Kato, and Y. Motome, *JPS Conf. Proc.* **30**, 011010 (2020).  
 [28] R. Takashima and S. Fujimoto, *J. Phys. Soc. Japan* **83**, 54717 (2014).



- [29] X.-X. Zhang, A. S. Mishchenko, G. De Filippis, and N. Nagaosa, *Phys. Rev. B* **94**, 174428 (2016).
- [30] X. Yu, A. Kikkawa, D. Morikawa, K. Shibata, Y. Tokunaga, Y. Taguchi, and Y. Tokura, *Phys. Rev. B* **91**, 054411 (2015).
- [31] S. Okumura, S. Hayami, Y. Kato, and Y. Motome, *Phys. Rev. B* **101**, 144416 (2020).
- [32] R. Ozawa, S. Hayami, and Y. Motome, *Phys. Rev. Lett.* **118**, 147205 (2017).
- [33] Y. Akagi, M. Udagawa, and Y. Motome, *Phys. Rev. Lett.* **108**, 096401 (2012).
- [34] R. Ozawa, S. Hayami, K. Barros, G. W. Chern, Y. Motome, and C. D. Batista, *J. Phys. Soc. Japan* **85**, 103703 (2016).
- [35] We adopt a slightly different definition for  $m_{\mathbf{Q}_\eta}$  from that in Ref. [31]; we take a symmetric summation with respect to  $\pm\mathbf{Q}_\eta$ , which results in just a difference of factor  $\sqrt{2}$ .